# Electron correlations and superconductivity in $La_3Ni_2O_7$ under pressure tuning

Zhiguang Liao,[1,*] Lei Chen,[2,*] Guijing Duan,[1,*] Yiming Wang,[2] Changle Liu,[3,4] Rong Yu,[1,5,†] and Qimiao Si[2,‡]

[1]*Department of Physics and Beijing Key Laboratory of Optoelectronic Functional Materials & Micro-Nano Devices, Renmin University of China, Beijing 100872, China*

[2]*Department of Physics & Astronomy, Rice Center for Quantum Materials, Rice University, Houston, Texas 77005, USA*

[3]*School of Engineering, Dali University, Dali, Yunnan 671003, China*

[4]*Shenzhen Institute for Quantum Science and Technology and Department of Physics, Southern University of Science and Technology, Shenzhen 518055, China*

[5]*Key Laboratory of Quantum State Construction and Manipulation (Ministry of Education), Renmin University of China, Beijing 100872, China*

(Received 31 August 2023; revised 5 December 2023; accepted 6 December 2023; published 28 December 2023)

Motivated by the recent discovery of superconductivity in $La_3Ni_2O_7$ under pressure, we discuss the basic ingredients of a model that captures its microscopic physics under pressure tuning. We anchor our description in terms of the spectroscopic evidence of strong correlations in this system. In a bilayer Hubbard model including the Ni $3d$ $x^2-y^2$ and $z^2$ orbitals, we show the ground state of the model crosses over from a low-spin $S=1/2$ state to a high-spin $S=3/2$ state. In the high-spin state, the two $x^2-y^2$ and the bonding $z^2$ orbitals are all close to half-filling, which promotes a strong orbital selectivity in a broad crossover regime of the phase diagram pertinent to the system. Based on these results, we construct an effective multiorbital $t$-$J$ model to describe the superconductivity of the system, and find the leading pairing channel to be an intraorbital spin singlet with a competition between the extended $s$-wave and $d_{x^2-y^2}$ symmetries. Our results highlight the role of strong multiorbital correlation effects in driving the superconductivity of $La_3Ni_2O_7$.

DOI: 10.1103/PhysRevB.108.214522

## I. INTRODUCTION

The discovery of iron-based superconductors more than a decade ago provided hope for high temperature superconductivity in a variety of transition-metal-based materials [1–3]. The recent discovery of superconductivity in the bilayer Ni-based compound $La_3Ni_2O_7$, with a transition temperature of about 80 K when the applied pressure exceeds 14 GPa [4], was soon confirmed [5] and zero resistivity was recently obtained [6]. Unlike the infinite-layer nickelate $(Sr, Nd)NiO_2$ thin films [7], which was expected to resemble the physics of the cuprates given the valence count of $Ni^{1+}$ with a $d^9$ electron configuration, a simple valence count gives $Ni^{2.5+}$ in the bilayer compound $La_3Ni_2O_7$, corresponding to $d^{7.5}$. These results have naturally attracted extensive interest [8–22].

Some of the key questions concern the roles of multiple orbitals and electron correlations [23] for both the normal state and superconductivity of $La_3Ni_2O_7$. The first-principles density functional theory (DFT) calculation [4] shows that the bands near the Fermi level have mainly Ni $e_g$ orbital characters; bands with $t_{2g}$ orbital characters are located about 2 eV below the Fermi level. It also reveals a strong interlayer hopping between the two Ni $z^2$ orbitals through the apical oxygen ion, which leads to the formation of bonding-antibonding molecular orbitals (MOs) as illustrated in Fig. 1(a). Considering DFT results and the simple valence count, a naive picture of the electron state is as follows: Within a two-Ni unit cell, the $t_{2g}$ orbitals are almost fully occupied, and the four $e_g$ molecular orbitals are occupied by three electrons. To make progress, it is important to understand the exact ground-state configuration and the low-energy electronic degrees of freedom that underlie the normal state and are responsible for the superconductivity.

In this paper, we address these important issues by studying the electron correlations in a bilayer two-orbital Hubbard model for $La_3Ni_2O_7$. Importantly, we anchor our description in terms of the spectroscopically derived experimental evidence for strong correlations [23]. One of our key findings is to show that the electron correlations drive the ground state from a low-spin $S=1/2$ configuration to a high-spin $S=3/2$ one. In the broad crossover regime of the phase diagram, the system exhibits strong orbital selectivity. This regime falls in the parameter range pertinent to $La_3Ni_2O_7$, as highlighted in Fig. 1(b). We clarify the nature of this crossover regime by showing that further increasing the interaction strength stabilizes an orbital-selective Mott phase (OSMP) in which the two $x^2-y^2$ orbitals are Mott localized whereas the $z^2$ orbitals remain itinerant: Thus, a *proximity* to the OSMP underlies the strong orbital selectivity seen in the crossover regime. Our results provide the natural understanding of the recent optical conductivity experiments, which provided evidence that the

*These authors contributed equally to this work.
†rong.yu@ruc.edu.cn
‡qmsi@rice.edu

 

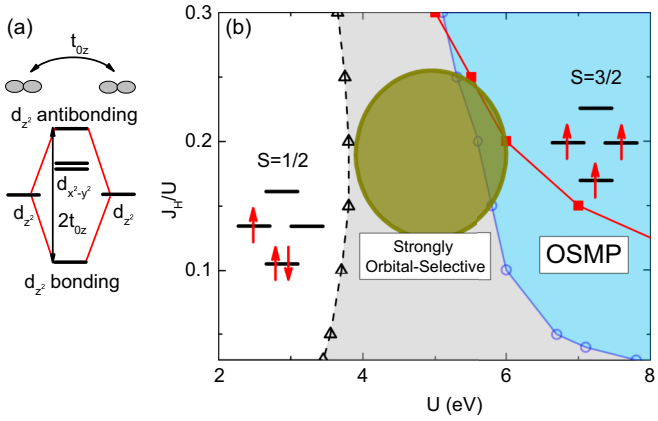


FIG. 1. (a) Sketch of formation of the bonding-antibonding MO states between the Ni $z^2$ orbitals in the top and bottom layers. (b) Ground-state phase diagram in the $U$-$J_H$ plane of the bilayer two-orbital Hubbard model for $La_3Ni_2O_7$, calculated by the $U(1)$ slave-spin theory in the MO basis. The red line with squares shows the transition between the low-spin $S = 1/2$ state and the high-spin $S = 3/2$ state in the atomic limit. The blue regime is the orbital-selective Mott phase (OSMP) in which the $x^2 - y^2$ orbitals are Mott localized whereas the $z^2$ orbitals are itinerant [see Fig. 3(a)]. The dashed line with triangles characterizes the low-spin to high-spin crossover, and in the gray regime the system exhibits strong orbital selectivity (see text). Highlighted by the golden shading in the plot is the parameter region pertinent to $La_3Ni_2O_7$.

electrons' kinetic energy is less than 0.1 of its noninteracting counterpart [23] and that the Drude peak contains two components [23]. Our results on the correlation effect, in turn, allow us to advance the low-energy physics that drives the superconductivity.

## II. MODEL AND METHOD

We consider a bilayer multiorbital Hubbard model for the two $e_g$ orbitals of Ni: $H = H_{\rm TB} + H_{\rm int}$. Here, $H_{\rm TB}$ is a tight-binding Hamiltonian,

$$H_{\rm TB} = \frac{1}{2}\sum_{i\delta_{n(z)}\alpha\beta\sigma} t^{\alpha\beta}_{\delta_{n(z)}} d^\dagger_{i\alpha\sigma} d_{i+\delta_{n(z)}\beta\sigma} + \sum_{i\alpha\sigma}(\epsilon_\alpha - \mu) d^\dagger_{i\alpha\sigma} d_{i\alpha\sigma}, \tag{1}$$

where $d^\dagger_{i\alpha\sigma}$ creates an electron in orbital $\alpha$ ($\alpha = x, z$ denoting the two $e_g$ orbitals, $x^2 - y^2$ and $z^2$, respectively) with spin $\sigma$ at site $i$ of a bilayer square lattice, $\delta_{n(z)}$ denotes the $n$th neighboring site in the same (opposite) layer, $\epsilon_\alpha$ refers to the energy level associated with the crystal field splittings, and $\mu$ is the chemical potential. The tight-binding parameters $t^{\alpha\beta}_{\delta_{n(z)}}$ and $\epsilon_\alpha$, which are summarized in Table I, are obtained by fitting the calculated DFT band structure and projecting to the two-$e_g$-orbital basis in a unit cell including two Ni sites as described in detail in Appendix A. Note that for simplification we have used a tetragonal lattice structure in the DFT calculation, as explained in the Appendix. To avoid confusion, in band structure results, we also list names of high-symmetry points corresponding to the actual structure of the compound. We adjust the chemical potential so that the total electron density is 3 per unit cell to reflect the valence count of $Ni^{2.5+}$. The on-site interaction $H_{\rm int}$ reads

$$\begin{aligned} H_{\rm int} = {} & \frac{U}{2}\sum_{i,\alpha,\sigma} n_{i\alpha\sigma} n_{i\alpha\bar\sigma} \\ & + \sum_{i,\alpha<\beta,\sigma} \{U' n_{i\alpha\sigma} n_{i\beta\bar\sigma} + (U' - J_{\rm H}) n_{i\alpha\sigma} n_{i\beta\sigma} \\ & - J_{\rm H}(d^\dagger_{i\alpha\sigma} d_{i\alpha\bar\sigma} d^\dagger_{i\beta\bar\sigma} d_{i\beta\sigma} + d^\dagger_{i\alpha\sigma} d^\dagger_{i\alpha\bar\sigma} d_{i\beta\sigma} d_{i\beta\bar\sigma})\}, \end{aligned} \tag{2}$$

where $n_{i\alpha\sigma} = d^\dagger_{i\alpha\sigma} d_{i\alpha\sigma}$. Here, $U$, $U'$, and $J_{\rm H}$, respectively denote the intra- and interorbital repulsion and the Hund's rule coupling, and $U' = U - 2J_{\rm H}$ is used [24].

As already mentioned, the strong hopping between the two Ni $z^2$ orbitals in the upper and lower layers causes bonding-antibonding MO states. To examine this bonding effect, we perform a transformation from the atomic orbital basis to the bonding MO basis, namely by defining the MO as

$$d^{b(a)}_{i\alpha\sigma} = \frac{1}{\sqrt{2}}(d_{i\alpha\sigma} \pm d_{i+\delta_{0z}\alpha\sigma}), \tag{3}$$

where the index $b(a)$ corresponds to the bonding (antibonding) MO, and $i$ ($i + \delta_{0z}$) on the right-hand side refers to a site in the top (bottom) layer. Note that we define MOs for both $z^2$ and $x^2 - y^2$ orbitals for convenience, though the $x^2 - y^2$ orbital is expected to be largely nonbonding given the small interlayer hopping amplitude associated with this orbital as shown in Table I. We can rewrite the tight-binding and interaction Hamiltonians of Eqs. (1) and (2) in the MO basis. In particular,

$$H_{\rm int} = H^{\rm b\text{-}b}_{\rm int} + H^{\rm b\text{-}a}_{\rm int}, \tag{4}$$

where $H^{\rm b\text{-}b}_{\rm int}$ refers to the interactions between bonding (or antibonding) states, whereas $H^{\rm b\text{-}a}_{\rm int}$ refers to the interactions mixing the bonding and antibonding states. The exact forms of $H^{\rm b\text{-}b}_{\rm int}$ and $H^{\rm b\text{-}a}_{\rm int}$ are presented in Appendix B.

The correlation effects of the above model in the MO basis are then investigated by using a $U(1)$ slave-spin theory [25,26]. In this approach, the $d$-electron operators are rewritten as $d^\dagger_{i\alpha\sigma} = S^+_{i\alpha\sigma} f^\dagger_{i\alpha\sigma}$ (here we absorb the MO index in $\alpha$), where $S^+_{i\alpha\sigma}$ ($f^\dagger_{i\alpha\sigma}$) is a quantum $S = 1/2$ spin (fermionic spinon) operator introduced to carry the electron's charge (spin) degree of freedom, and $S^z_{i\alpha\sigma} = f^\dagger_{i\alpha\sigma} f_{i\alpha\sigma} - \frac{1}{2}$ is a local constraint. At the saddle-point level, we employ a Lagrange multiplier $\lambda_\alpha$ to handle the constraint, and decompose the

TABLE I. Tight-binding parameters of the bilayer two-orbital model for $La_3Ni_2O_7$. $xx$ ($zz$) denotes the intraorbital hopping between the $x^2 - y^2$ ($z^2$) orbitals, whereas $xz$ denotes the interorbital hopping between the $x^2 - y^2$ and $z^2$ orbitals. $t_{n(z)}$ refers to intralayer (interlayer) hopping between the $n$th neighboring sites. Finally, $\pm$ means that the hopping parameter is positive along the $x$ direction but negative along the $y$ direction. All units are in eV.

| Orbital | $\epsilon$ | $t_1$ | $t_2$ | $t_3$ | $t_{0z}$ | $t_{1z}$ |
|---|---|---|---|---|---|---|
| $xx$ | 10.8735 | −0.4899 | 0.0670 | −0.0600 | 0.0022 | 0.0003 |
| $zz$ | 10.5142 | −0.1159 | −0.0109 | −0.0187 | −0.6363 | 0.0231 |
| $xz$ | | $\mp$0.2420 | 0 | $\mp$0.0333 | 0 | $\pm$0.0382 |

slave-spin and spinon operators. In this way, the model rewritten in the slave-spin representation is solved by determining $\lambda_\alpha$ and the quasiparticle spectral weight $Z_\alpha \propto |\langle S_\alpha^+ \rangle|^2$ self-consistently [25,26].

## III. LOW-SPIN TO HIGH-SPIN CROSSOVER AND ORBITAL-SELECTIVE MOTT PHYSICS

We first diagonalize the interaction Hamiltonian of Eq. (4) in the MO basis. The ground state is either a low-spin $S = 1/2$ state at small $J_H$ or a high-spin $S = 3/2$ state at large $J_H$, as shown in Appendix B. In the low-spin state, the $z^2$ bonding state is largely doubly occupied, whereas the antibonding state is almost empty. The $x^2 - y^2$ orbitals are near quarter filling. In the high-spin state, on the other hand, the bonding $z^2$ and $x^2 - y^2$ orbitals are all half filled, and the antibonding $z^2$ state stays empty. Either the low-spin or the high-spin configuration is fourfold degenerate. For the low-spin state, the additional degeneracy comes from the doubly degenerate $x^2 - y^2$ orbitals, which can be described by an isospin $\tau = 1/2$. The transition from the low-spin to high-spin state is shown as the red line with square symbols in Fig. 1(b). In the presence of electron hopping, this transition turns into a crossover.

To examine how this crossover takes place in the multiorbital Hubbard model, we perform slave-spin calculation in the MO basis. Note that the antibonding $z^2$ state has a very low electron density $n < 0.1$ at $U = 0$. Accordingly, we expect it to be only weakly affected by interactions. To simplify the calculation, we set $Z = 1$ in this MO and turn off interaction terms associated with this orbital. The results of the slave-spin calculation is summarized in the phase diagram of Fig. 1(b). In this figure, the dashed line characterizes the low-spin to high-spin crossover. Here we note that the crossover is actually a very broad regime. To see this, we define the variances of the electron density profile from that dominating the low- and high-spin states in the atomic limit:

$$\sigma_L^2 = \tfrac{1}{4}\big[(n_{z^2(b)} - 1)^2 + (n_{z^2(a)})^2 + 2(n_{x^2-y^2} - 1/4)^2\big],$$
$$\sigma_H^2 = \tfrac{1}{4}\big[(n_{z^2(b)} - 1/2)^2 + (n_{z^2(a)})^2 + 2(n_{x^2-y^2} - 1/2)^2\big]. \quad (5)$$

The variances with $U$ at $J_H/U = 0.25$ is depicted in Fig. 2. It is clearly seen that the system deviates from either the ideal low- or high-spin state within a wide range of $U$ values. To be precise, in the phase diagram of Fig. 1(b), the low-spin to high-spin crossover is determined by the criterion $\sigma_H^2 = \sigma_L^2$.

Across this crossover line with increasing $U$ to the gray regime, the system exhibits strong orbital selectivity: As shown in Fig. 3(a), quasiparticle spectral weights and electron densities in all orbitals change drastically and $Z_{x^2-y^2} \ll Z_{z^2}$ in this regime. Further increasing $U$, the system undergoes an orbital-selective Mott transition (OSMT) to an OSMP at the blue line with circles. As shown in Fig. 3, in the OSMP $Z_{x^2-y^2} = 0$ and $n_{x^2-y^2} = 1/2$, but $Z_{z^2(b)} > 0$: The electrons in the $x^2 - y^2$ orbitals are Mott localized whereas those in the $z^2$ bonding states are still itinerant, though very close to the Mott localization.

The OSMP is associated with the high-spin state. One sees from Fig. 3(b) that in this state the electron densities of the $x^2 - y^2$ and $z^2$ bonding orbitals are all close to 1/2. If the antibonding state were to be completely empty, the system consisting of the other three orbitals would be exactly at half filling and would become Mott insulating when the red line of transition in Fig. 1(b) is approached. However, at finite $U$ an OSMP is more favorable because keeping the $z^2$ bonding orbital itinerant reduces the kinetic energy. This naturally explains why the OSMT line almost traces the red transition line to the high-spin Mott insulator (MI), especially when $J_H/U$ is large.

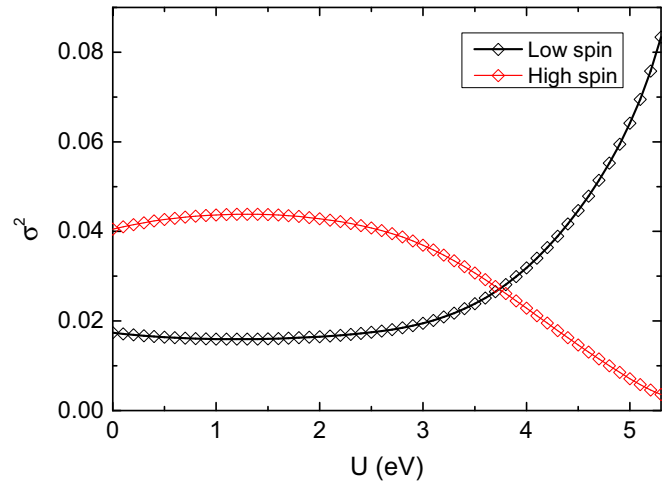


FIG. 2. Variance of the electron density profile from the low-spin and high-spin states at $J_H/U = 0.25$. The low-spin to high-spin crossover is determined from the crossing point of the two variance curves.

We next consider the effects of orbital-selective Mott correlations to the electronic structure. Figure 4(a) shows the bands along high-symmetry directions of the Brillouin zone at $U = 5.3$ eV compared to those at $U = 0$. Close to the OSMP, bands with the $x^2 - y^2$ and $z^2$ bonding orbital characters are strongly renormalized whereas the $z^2$ antibonding band, located topmost in energy, hardly shifts compared to the $U = 0$ case. As shown in Figs. 4(b) and 4(c), compared to the significant renormalization in the total bandwidth $W$ from about 4 eV to about 1.5 eV, the Fermi surface only changes moderately. While the relatively small inner hole pocket centered at the $M$ point exhibits a sizable expansion, the outer hole and electron pockets centered around the $\Gamma$ point only slightly shrink and expand, respectively.

## IV. AN EFFECTIVE MULTIORBITAL *t*-*J* MODEL FOR SUPERCONDUCTIVITY

The above slave-spin results set the stage to build a low-energy effective model to understand superconductivity of the system, which can be done by performing a $t/U$ perturbation expansion when $U$ is sizable. However, the resulting form of the effective theory depends on the low-energy manifold the perturbed Hamiltonian is projected to. For example, when projecting to the $S = 1/2$ low-spin sector, one ends up with an effective model that includes interactions between the total spin and isospin operators, which takes the form of the Kugel-Khomskii model [27]. On the other hand, one obtains three-orbital Heisenberg couplings for the interacting part of the Hamiltonian when projecting to the high-spin sector.

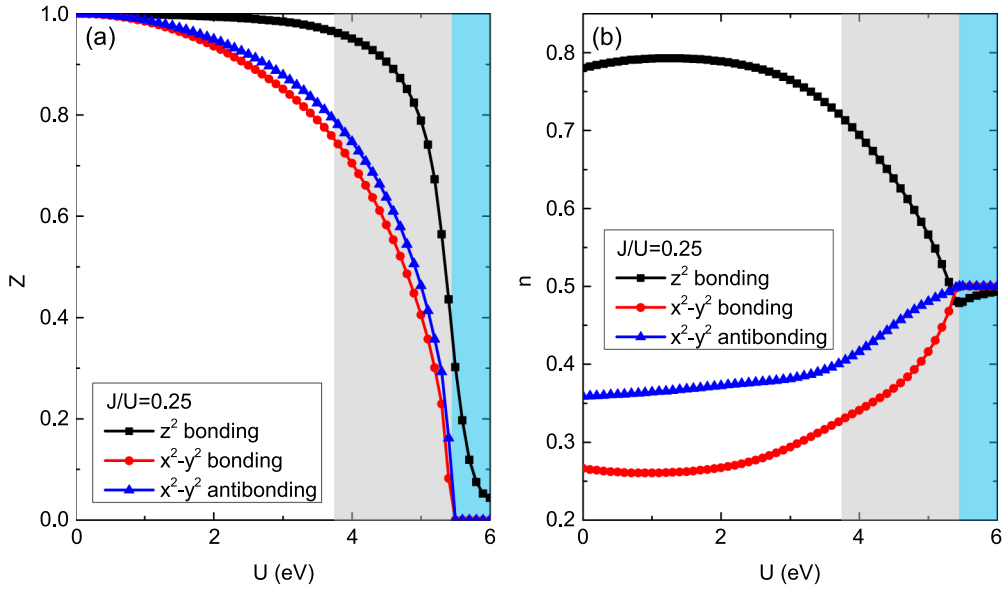


FIG. 3. Evolution of the orbital-resolved quasiparticle spectral weight $Z$ [in (a)] and electron density $n$ [in (b)] with increasing $U$ at $J_H/U = 0.25$ of the bilayer two-orbital model in the MO basis calculated by using the $U(1)$ slave-spin theory. The blue and gray regimes correspond to OSMP and metallic state with strong orbital selectivity, respectively.

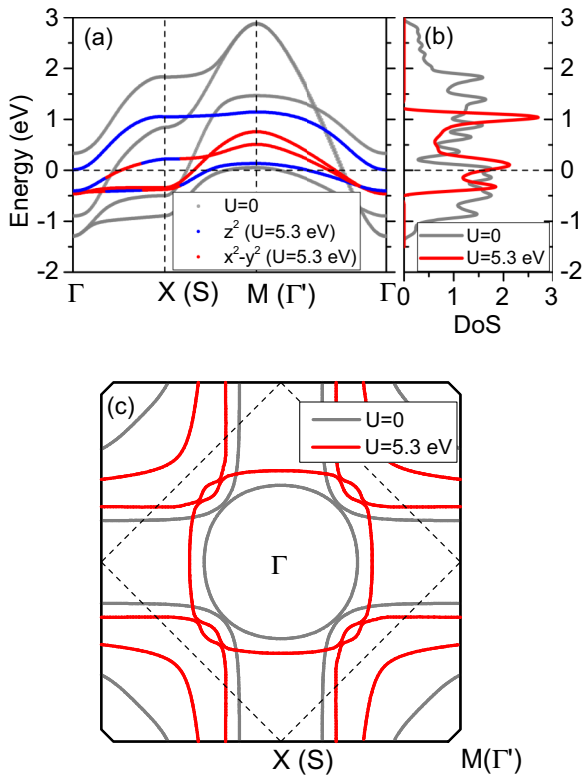


FIG. 4. (a) Band structure at $U = 5.3$ eV compared to the one at $U = 0$, indicating strong orbital-selective band renormalization. (b) The corresponding electron density of states (DoS) showing a large renormalization on the bandwidth $W$. (c) Comparison of the Fermi surface at $U = 5.3$ eV and $U = 0$. In the calculation, we have used a simplified tetragonal structure. The BZ corresponding to the orthorhombic structure of the compound is shown as dashed lines in panel (c), and the corresponding names of the high-symmetry points in this BZ are given in parentheses. $\Gamma'$ refers to the $\Gamma$ point of the second BZ.

Which model is pertinent to the low-energy physics depends on the strength of the interaction.

For $La_3Ni_2O_7$, $U$ is estimated to be within 4 to 6 eV [4,10]. According to the phase diagram in Fig. 1(b), this suggests that the system is in the regime with strong orbital selectivity near the OSMP [as highlighted in Fig. 1(b)]. Therefore, we construct the effective model by starting from the $S = 3/2$ high-spin ground state and taking into account effects of the $S = 1/2$ low-lying excitations by projecting out doubly occupied states. As a result, it takes the form of a multiorbital $t$-$J$ model where the Hamiltonian reads

$$H_{\text{eff}} = \frac{1}{2}\sum_{ij\alpha\beta\sigma}\sqrt{Z_\alpha Z_\beta}t_{ij}^{\alpha\beta}f_{i\alpha\sigma}^\dagger f_{j\beta\sigma} + \sum_{i\alpha\sigma}(\epsilon'_\alpha - \mu)f_{i\alpha\sigma}^\dagger f_{i\alpha\sigma} + {\sum_{ij\alpha\beta}}' J_{ij}^{\alpha\beta}\mathbf{S}_{i\alpha}\cdot\mathbf{S}_{j\beta}. \quad (6)$$

Here we have employed the slave-spin method to renormalize the kinetic part of the Hamiltonian; $Z_\alpha$ is the quasiparticle spectral weight of the $\alpha$th MO, and $\epsilon'_\alpha$ refers to the renormalized energy level of orbital $\alpha$. This is a generalization of the slave-boson theory [28] to the finite $U$ case. $\mathbf{S}_{i\alpha} = \frac{1}{2}f_{i\alpha s}^\dagger \boldsymbol{\sigma}_{ss'} f_{i\alpha s'}$ denotes the spin density operator at site $i$ in the $\alpha$ orbital. Considering the high-spin state, the summation $\sum'$ runs over the two $x^2-y^2$ and the one $z^2$ bonding MOs. $J_{ij}^{\alpha\beta}$ refers to the orbital dependent exchange coupling which can be determined from the second-order $t/U$ perturbation expansion, as detailed in Appendix C. Here we neglect the interlayer couplings between $x^2-y^2$ orbitals and second-nearest and further neighboring interactions because of their small hopping amplitudes, and only consider the in-plane nearest neighboring exchange interactions $J_1^{xx}$, $J_1^{zz}$, and $J_1^{xz}$. We find $J_1^{xz}$ to be negligibly small, and $J_1^{xx}$, $J_1^{zz}$ are antiferromagnetic. In the following, we take the convention $J^{\alpha\beta}$ for $J_1^{\alpha\beta}$. To explore how the superconducting pairing evolves with

TABLE II. Superconducting pairing symmetry of the effective multiorbital $t$-$J$ model. $\Delta(\mathbf{r})$ and $\Delta(\mathbf{k})$ refer to gap functions in real and momentum space, respectively. Their symmetry is characterized by the corresponding irreducible representation of the tetragonal $D_{4h}$ group. $\eta_0$ and $\eta_3$ refer to the $2\times 2$ unit marix and $z$ component of the Pauli matrix, respectively. $\hat{x}$ ($\hat{y}$) refers to unit vector along the $x$ ($y$) direction.

| Orbital | $\Delta(\mathbf{r})$ | $\Delta(\mathbf{k})$ | Symmetry |
|---|---|---|---|
| $x^2-y^2$ | $(\Delta_{\hat{x}}+\Delta_{\hat{y}})\eta_0$ | $s_{x^2+y^2}\eta_0$ | $A^{1g}$ |
| | $(\Delta_{\hat{x}}-\Delta_{\hat{y}})\eta_0$ | $d_{x^2-y^2}\eta_0$ | $B^{1g}$ |
| | $(\Delta_{\hat{x}}+\Delta_{\hat{y}})\eta_3$ | $s_{x^2+y^2}\eta_3$ | $A^{2u}$ |
| | $(\Delta_{\hat{x}}-\Delta_{\hat{y}})\eta_3$ | $d_{x^2-y^2}\eta_3$ | $B^{2u}$ |
| $z^2$ | $\Delta_{\hat{x}}+\Delta_{\hat{y}}$ | $s_{x^2+y^2}$ | $A^{1g}$ |
| | $\Delta_{\hat{x}}-\Delta_{\hat{y}}$ | $d_{x^2-y^2}$ | $B^{1g}$ |

orbital-selective correlations, we take $J^{zz}=0.025W_0$ (with $W_0$ referring to the bandwidth at $U=0$), and tune the ratio $r=J^{xx}/J^{zz}$.

## V. SUPERCONDUCTING PAIRING SYMMETRY

The superconducting pairing in the model of Eq. (6) is studied by a Bogoliubov mean-field decomposition of the exchange interactions in the intraorbital spin singlet sector:

$$J_\delta^{\alpha\alpha}\left(\mathbf{S}_{i\alpha}\cdot\mathbf{S}_{i+\delta\alpha}-\frac{1}{4}n_{i\alpha}n_{i+\delta\alpha}\right)$$
$$\approx -\frac{J_\delta^{\alpha\alpha}}{2}\left(\hat{\Delta}_{\delta\alpha}^{\dagger}\Delta_{\delta\alpha}+\text{H.c.}-|\Delta_{\delta\alpha}|^2\right), \tag{7}$$

where $\hat{\Delta}_{\delta\alpha}=f_{i\alpha\downarrow}f_{i+\delta\alpha\uparrow}-f_{i\alpha\uparrow}f_{i+\delta\alpha\downarrow}$, and the gap function $\Delta_{\delta\alpha}=\langle\hat{\Delta}_{\delta\alpha}\rangle$. $La_3Ni_2O_7$ under pressure has an orthorhombic structure. But the difference between the $a$ and $b$ lattice constants is small (about 1%) [4]. As such, for convenience, we examine the symmetry of the gap functions by studying how they transform under the tetragonal $D_{4h}$ group. The result is summarized in Table II. One sees that the multiorbital nature leads to six different pairing channels. We then perform a self-consistent calculation to determine the leading pairing channel [29]. As shown in Fig. 5, the leading pairing channel changes from the extended $s$-wave $A_{z^2}^{1g}$ to $d$-wave $B^{1g}$ in both $x^2-y^2$ and $z^2$-bonding orbitals with increasing $J^{xx}$. In the $A^{1g}$ dominant regime, the pairing is also strongly orbital selective, with the leading channel associated with the $z^2$ bonding orbital. Besides the larger pairing amplitude stabilized by $J^{zz}$, this pairing channel is also favored by causing a full superconducting gap along the inner hole pocket centered at the $M$ point. However, nodes along the outer hole pocket cannot be avoided by either pairing channel. To avoid nodes, it is possible that a pairing function with mixed $s$- and $d$-wave characters, such as the time-reversal breaking $s+\mathrm{i}d$ [29] or $s+d$ (given the orthorhombic lattice symmetry of the compound) [30], is stabilized in the regime where $A^{1g}$ and $B^{1g}$ pairing channels are in competition.

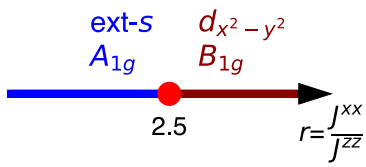


FIG. 5. Evolution of the leading superconducting pairing symmetry, from an extended $s$-wave $A^{1g}$ to a $d$-wave $B^{1g}$ with increasing $J^{xx}$. Here we take $J^{zz}=0.025W_0$, and vary the ratio $r=J^{xx}/J^{zz}$, where $W_0$ is the total bandwidth of the multiorbital Hubbard model at $U=0$.

## VI. DISCUSSIONS AND CONCLUSIONS

Several remarks are in order. First, the OSMP found in our model for $La_3Ni_2O_7$ shares some similarity to that of the iron-based superconductors [31], for which extensive evidence has come from angle-resolved photoemission [32,33] and other measurements [3]. In both systems, the OSMP is stabilized when the electron filling of each relevant orbital is either at or slightly away from half filling. This justifies the reduction from the multiorbital Hubbard model to the $t$-$J$ one. Second, as shown in Fig. 3(a), very close and inside the OSMP the overall quasiparticle spectral weight is less than 0.1. This causes the system to be in proximity to an OSMP, which naturally explains the substantially suppressed Drude weight (with the renormalized electrons' kinetic energy ratio less than 0.1) as observed in a recent optical conductivity measurement [23]. The strong orbital selectivity between the $z^2$ and $x^2-y^2$ orbitals accounts for the observed two-component contribution to the Drude weight [23]. Third, applying a pressure corresponds to increasing the hopping amplitudes, or equivalently, reducing the $U/t$ ratio in our model. This increases the itinerancy of electrons, and causes bandwidth tuning of the superconductivity. But in multiorbital systems reducing the $U/t$ ratio has additional effects. It can trigger a high-spin to low-spin crossover, as shown in the present work. This activates the orbital degree of freedom, which makes the exchange couplings orbital dependent and may lead to strong competition of fluctuations in the antiferromagnetic spin and orbital channels, as reflected in the complicated temperature evolution of the magnetic susceptibility in $La_3Ni_2O_7$ at ambient pressure [34,35]. Moreover, reducing the $U/t$ ratio also causes redistribution of the electrons among the orbitals, leading to an effect similar to either hole or electron doping a MI in each orbital. This effect resembles a multiorbital version of the physics in doping the cuprates, which is known to favor superconductivity.

In conclusion, we have studied electron correlation effects in a bilayer two-orbital Hubbard model for $La_3Ni_2O_7$ in the MO basis, and found a strong orbital selectivity when the interaction strength is moderate. Further increasing the interaction, an OSMP is stabilized. The OSMP is close to an $S=3/2$ high-spin state, in which the $x^2-y^2$ and $z^2$ bonding orbitals are all very close to half filling. In light of these results, we obtain an effective multiorbital $t$-$J$ model for superconductivity of the system in the crossover regime towards the high-spin configuration. We show that the system exhibits orbital-selective pairing and the leading superconducting pairing channel evolves from the extended $s$-wave $A^{1g}$ to $d$-wave $B^{1g}$ when the intraorbital nearest-neighbor exchange coupling $J^{xx}$ is increased. Our work paves the way for systematically

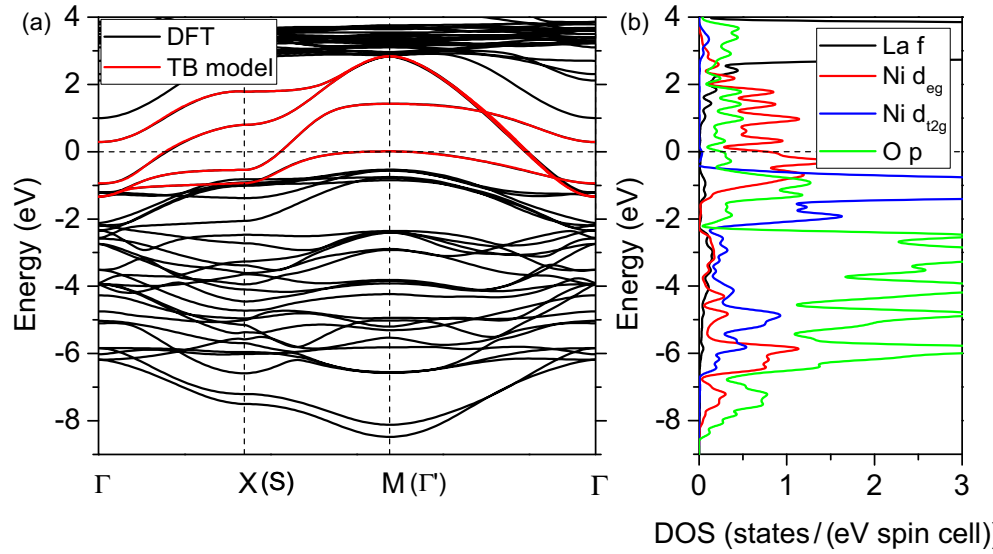


FIG. 6. (a) Band structure of $La_3Ni_2O_7$ along high-symmetry directions of the BZ calculated from DFT (black lines) and from the bilayer two-orbital tight-binding model (red lines). (b) The corresponding projected DoS calculated from DFT. In the calculation, we have used a simplified tetragonal structure. The corresponding names of the high-symmetry points in the actual orthorhombic structure of the compound BZ are given in brackets. $\Gamma'$ refers to the $\Gamma$ point of the second BZ.

describing the pressure-induced high-$T_c$ superconductivity of $La_3Ni_2O_7$.

## ACKNOWLEDGMENTS

We acknowledge H. Hwang, E. M. Nica, C. Varma, M. Wang, H.-H. Wen, and W. Yu for useful discussions. This work was supported in part by the National Science Foundation of China (Grants No. 12334008 and No. 12174441). Work at Rice University was primarily supported by the U.S. Department of Energy, Office of Science, Basic Energy Sciences, under Award No. DE-SC0018197, and by the Robert A. Welch Foundation Grant No. C-1411. Q.S. acknowledges the hospitality of the Aspen Center for Physics, which is supported by NSF Grant No. PHY-2210452, during the workshop "New directions on strange metals in correlated systems."

## APPENDIX A: DETAILS ON THE TIGHT-BINDING MODEL

To include the realistic band structure at low energies to our tight-binding modeling, we first carried out band structure calculations for $La_3Ni_2O_7$ within the framework of DFT. We have used the plane wave basis set as implemented in the Vienna Ab initio Simulation Package (VASP) code [36]. Projector augmented-wave potentials and the Perdew-Burke-Ernzerhof exchange-correlation functional were used in the calculations. We consider the experimental lattice parameters ($a = 5.289$ Å, $b = 5.218$ Å, $c = 19.734$ Å) [4] in the simulations. Since the difference between $a$ and $b$ is only about 1.3%, we use their average value ($a = b = 5.2535$ Å) in the calculations. Though this procedure has modified the space group from $Fmmm$ to $I4/mmm$, it should have little effect on the electronic structure.

As shown in Fig. 6, the bands near the Fermi energy have mainly the Ni $3d$ $e_g$ orbital character. The bands associated with the $t_{2g}$ orbitals are at least 1 eV below the Fermi level. The oxygen $2p$ bands are dominant at about 4 eV below the Fermi energy. Therefore, the relevant orbitals within a 2 eV energy window about the Fermi energy are the Ni $e_g$ ones. We hence fit the Wannierized bands with a bilayer two-orbital tight-banding Hamiltonian including these $e_g$ orbitals in the BZ corresponding to the two Ni (in the top and bottom layers) unit cells. At this step we have used projected Wannier functions; the procedure of disentanglement was performed with the maximally localized Wannier functions scheme as implemented in the WANNIER90 code [37]. The tight-binding parameters from the fitting are summarized in Table I.

The band structure of the bilayer two-orbital tight-binding model compared to the DFT results is shown in Fig. 6. The tight-binding model reproduces a similar band structure of DFT in the energy window of interest, from $-1.5$ to 2.5 eV.

## APPENDIX B: THE INTERACTION HAMILTONIAN IN THE BONDING MOLECULAR ORBITAL BASIS AND THE LOW-SPIN TO HIGH-SPIN CROSSOVER

In Eq. (3), we performed a transformation from the atomic orbital basis to the MO basis. Here we define MOs for both the $z^2$ and $x^2 - y^2$ orbitals for convenience. But, as listed in Table I, the interlayer hopping amplitude between the $x^2 - y^2$ orbitals is much smaller than both its intralayer counterpart and the interlayer hopping between the $z^2$ orbitals. We therefore expect that the $x^2 - y^2$ orbital is largely nonbonding.

In this MO basis, the interaction Hamiltonian is rewritten to

$$H_{\rm int} = H_{\rm int}^{\rm b\text{-}b} + H_{\rm int}^{\rm b\text{-}a}, \tag{B1}$$

where the boning-bonding and antibonding-antibonding interactions are

$$H_{\text{int}}^{\text{b-b}} = \frac{U}{2}\sum_{\alpha}\left(n^a_{I\alpha\uparrow}n^a_{I\alpha\downarrow}+n^b_{I\alpha\uparrow}n^b_{I\alpha\downarrow}\right)+\frac{U'}{4}\sum_{\alpha\neq\beta,\sigma\neq\sigma'}\left(n^a_{I\alpha\sigma}n^a_{I\beta\sigma'}+n^b_{I\alpha\sigma}n^b_{I\beta\sigma'}\right)$$
$$+\frac{U'-J}{2}\sum_{\alpha>\beta,\sigma}\left(n^a_{I\alpha\sigma}n^a_{I\beta\sigma}+n^b_{I\alpha\sigma}n^b_{I\beta\sigma}\right)-\frac{J}{2}\sum_{\alpha\neq\beta}\left(d^{a+}_{I\alpha\uparrow}d^{a+}_{I\beta\downarrow}d^{a}_{I\beta\uparrow}d^{a}_{I\alpha\downarrow}+d^{b+}_{I\alpha\uparrow}d^{b+}_{I\beta\downarrow}d^{b}_{I\beta\uparrow}d^{b}_{I\alpha\downarrow}\right)$$
$$-\frac{J}{2}\sum_{\alpha\neq\beta}\left(d^{b+}_{I\alpha\uparrow}d^{b+}_{I\alpha\downarrow}d^{b}_{I\beta\uparrow}d^{b}_{I\beta\downarrow}+d^{a+}_{I\alpha\uparrow}d^{a+}_{I\alpha\downarrow}d^{a}_{I\beta\uparrow}d^{a}_{I\beta\downarrow}\right), \tag{B2}$$

and the bonding-antibonding mixing interaction is

$$H_{\text{int}}^{\text{b-a}} = \frac{U}{2}\sum_{\alpha}\left(n^a_{I\alpha\uparrow}n^b_{I\alpha\downarrow}+n^b_{I\alpha\uparrow}n^a_{I\alpha\downarrow}\right)+\frac{U'}{4}\sum_{\alpha\neq\beta,\sigma\neq\sigma'}\left(n^a_{I\alpha\sigma}n^b_{I\beta\sigma'}+n^b_{I\alpha\sigma}n^a_{I\beta\sigma'}\right)+\frac{U'-J}{2}\sum_{\alpha>\beta,\sigma}\left(n^a_{I\alpha\sigma}n^b_{I\beta\sigma}+n^b_{I\alpha\sigma}n^a_{I\beta\sigma}\right)$$
$$+\frac{U}{2}\sum_{\alpha}\left(d^{b+}_{I\alpha\uparrow}d^{a}_{I\alpha\uparrow}d^{b+}_{I\alpha\downarrow}d^{a}_{I\alpha\downarrow}+d^{b+}_{I\alpha\uparrow}d^{a}_{I\alpha\uparrow}d^{a+}_{I\alpha\downarrow}d^{b}_{I\alpha\downarrow}+d^{a+}_{I\alpha\uparrow}d^{b}_{I\alpha\uparrow}d^{b+}_{I\alpha\downarrow}d^{a}_{I\alpha\downarrow}+d^{a+}_{I\alpha\uparrow}d^{b}_{I\alpha\uparrow}d^{a+}_{I\alpha\downarrow}d^{b}_{I\alpha\downarrow}\right)$$
$$+\frac{U'}{4}\sum_{\alpha\neq\beta,\sigma\neq\sigma'}\left(d^{b+}_{I\alpha\sigma}d^{a}_{I\alpha\sigma}d^{b+}_{I\beta\sigma'}d^{a}_{I\beta\sigma'}+d^{b+}_{I\alpha\sigma}d^{a}_{I\alpha\sigma}d^{a+}_{I\beta\sigma'}d^{b}_{I\beta\sigma'}+d^{a+}_{I\alpha\sigma}d^{b}_{I\alpha\sigma}d^{b+}_{I\beta\sigma'}d^{a}_{I\beta\sigma'}+d^{a+}_{I\alpha\sigma}d^{b}_{I\alpha\sigma}d^{a+}_{I\beta\sigma'}d^{b}_{I\beta\sigma'}\right)$$
$$+\frac{U'-J}{2}\sum_{\alpha>\beta,\sigma}\left(d^{b+}_{I\alpha\sigma}d^{a}_{I\alpha\sigma}d^{b+}_{I\beta\sigma}d^{a}_{I\beta\sigma}+d^{b+}_{I\alpha\sigma}d^{a}_{I\alpha\sigma}d^{a+}_{I\beta\sigma}d^{b}_{I\beta\sigma}+d^{a+}_{I\alpha\sigma}d^{b}_{I\alpha\sigma}d^{b+}_{I\beta\sigma}d^{a}_{I\beta\sigma}+d^{a+}_{I\alpha\sigma}d^{b}_{I\alpha\sigma}d^{a+}_{I\beta\sigma}d^{b}_{I\beta\sigma}\right)$$
$$-\frac{J}{2}\sum_{\alpha\neq\beta}\left(d^{a+}_{I\alpha\uparrow}d^{a+}_{I\beta\downarrow}d^{b}_{I\beta\uparrow}d^{b}_{I\alpha\downarrow}+d^{b+}_{I\alpha\uparrow}d^{b+}_{I\beta\downarrow}d^{a}_{I\beta\uparrow}d^{a}_{I\alpha\downarrow}+d^{b+}_{I\alpha\uparrow}d^{a+}_{I\beta\downarrow}d^{b}_{I\beta\uparrow}d^{a}_{I\alpha\downarrow}\right.$$
$$\left.+d^{b+}_{I\alpha\uparrow}d^{a+}_{I\beta\downarrow}d^{a}_{I\beta\uparrow}d^{b}_{I\alpha\downarrow}+d^{a+}_{I\alpha\uparrow}d^{b+}_{I\beta\downarrow}d^{b}_{I\beta\uparrow}d^{a}_{I\alpha\downarrow}+d^{a+}_{I\alpha\uparrow}d^{b+}_{I\beta\downarrow}d^{a}_{I\beta\uparrow}d^{b}_{I\alpha\downarrow}\right)$$
$$-\frac{J}{2}\sum_{\alpha\neq\beta}\left(d^{a+}_{I\alpha\uparrow}d^{a+}_{I\alpha\downarrow}d^{b}_{I\beta\uparrow}d^{b}_{I\beta\downarrow}+d^{b+}_{I\alpha\uparrow}d^{b+}_{I\alpha\downarrow}d^{a}_{I\beta\uparrow}d^{a}_{I\beta\downarrow}+d^{b+}_{I\alpha\uparrow}d^{a+}_{I\alpha\downarrow}d^{b}_{I\beta\uparrow}d^{a}_{I\beta\downarrow}\right.$$
$$\left.+d^{b+}_{I\alpha\uparrow}d^{a+}_{I\alpha\downarrow}d^{a}_{I\beta\uparrow}d^{b}_{I\beta\downarrow}+d^{a+}_{I\alpha\uparrow}d^{b+}_{I\alpha\downarrow}d^{b}_{I\beta\uparrow}d^{a}_{I\beta\downarrow}+d^{a+}_{I\alpha\uparrow}d^{b+}_{I\alpha\downarrow}d^{a}_{I\beta\uparrow}d^{b}_{I\beta\downarrow}\right). \tag{B3}$$

Diagonalizing the interaction Hamiltonian along with the on-site potential term in the tight-binding Hamiltonian written in the MO basis, we obtain two ground states in the atomic limit: an $S = 1/2$ low-spin state and an $S = 3/2$ high-spin state. These two ground states are illustrated in Fig. 7. Each state is fourfold degenerate. In the $S = 1/2$ low-spin state, the additional degeneracy is associated with the two degenerate $x^2 - y^2$ orbitals. As one sees, the low-spin configuration is dominated by the Fock state in which the bonding $z^2$ orbital is doubly occupied while the $x^2 - y^2$ orbitals are quarter filled. We can then define an orbital isospin operator $\boldsymbol{\tau}$, with the Ising variable $\tau^z$ denoting the electron density difference in the $x^2 - y^2$ orbitals between the top and bottom layers. The four degenerate low-spin configurations can be obtained from the one shown in Fig. 7 by applying total spin and orbital isospin reversal symmetry, respectively. On the other hand, the degenerate high-spin configurations can be labeled by the quantum number $S^z$ of the total spin. In the atomic limit, there is a transition from the low-spin to high-spin ground state by increasing $J_{\text{H}}$, shown as the red line in the phase diagram of Fig. 1(b). Taking into account the kinetic energy will turn the transition to a crossover.

## APPENDIX C: DETAILS ON THE DERIVATION OF THE EFFECTIVE MODEL

To construct the effective model, we start from the bilayer two-orbital Hubbard model in the MO basis, and rewrite the toal Hamiltonian in two parts, $H = H_0 + H_1$. We take the Hamiltonian in the atomic limit (including the interaction and on-site potential terms) as the unperturbed Hamiltonian $H_0$, and treat the hopping terms as perturbations ($H_1$). The effective low-energy model can be obtained via a canonical transformation,

$$\begin{aligned} H_{\text{eff}} &= e^{i\mathcal{S}}He^{-i\mathcal{S}} \\ &= H_0 + [i\mathcal{S}, H_0] + H_1 + [i\mathcal{S}, H_1] \\ &\quad + \tfrac{1}{2}[i\mathcal{S}, [i\mathcal{S}, H_0]] + \cdots . \end{aligned} \tag{C1}$$

The unitary operator $\mathcal{S}$ can be determined by requiring the first-order contribution in $H_1$ to be 0, and the effective Hamiltonian is derived from the second-order perturbation,

$$H_{\text{eff}} \approx \tfrac{1}{2}[i\mathcal{S}, H_1]. \tag{C2}$$

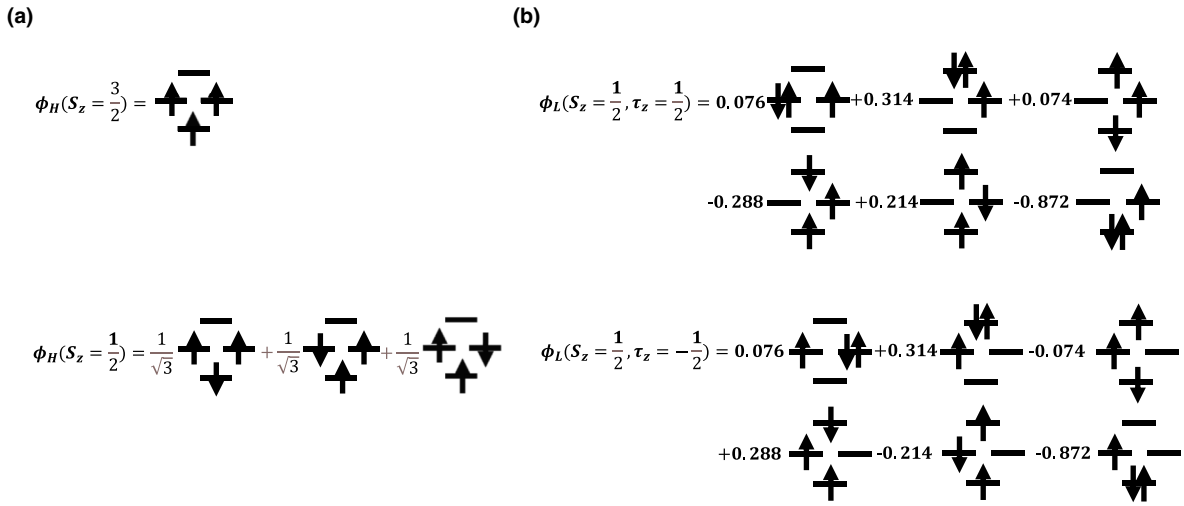


FIG. 7. (a) High-spin $S = 3/2$ ground-state configurations. (b) Low-spin $S = 1/2$ ground-state configurations. Each ground state is fourfold degenerate, and the other degenerate configurations can be obtained by reversing the spin direction ($S^z \to -S^z$) from those presented here.

We should then project the effective Hamiltonian onto the low-energy subspace, which is the high-spin $S = 3/2$ state in the strong-coupling limit $U/t \to \infty$. In this way, the effective model takes the form of an $S = 3/2$ Heisenberg model,

$$H_{\text{eff}} = \sum_{ij} J_{ij}\vec{S}_i \cdot \vec{S}_j, \tag{C3}$$

where $\vec{S}_i$ is the $S = 3/2$ spin operator at the $i$th unit cell. While this model should be well applied in the limit $U/t \to \infty$, calculations suggest the $La_3Ni_2O_7$ is close to the low-spin to high-spin crossover, where the effects of low-lying low-spin excitations are non-negligible. In practice, it would be difficult to project the effective Hamiltonian to a sector including both the high- and low-spin configurations given the incompatible quantum numbers of these two states. Here we adopt an alternative way. We consider a model with three-orbital Heisenberg couplings,

$$H_{\text{eff}} = \sum_{ij,\alpha\beta} J_{ij}^{\alpha\beta}\vec{S}_{i\alpha} \cdot \vec{S}_{j\beta} - \tilde{J}_{\text{H}} \sum_{i\alpha\beta} \vec{S}_{i\alpha} \cdot \vec{S}_{i\beta}, \tag{C4}$$

where $\vec{S}_{i\alpha}$ is an $S = 1/2$ spin operator in orbital $\alpha$, and $\alpha$ runs over the two $x^2 - y^2$ and the bonding $z^2$ orbitals. $\tilde{J}_{\text{H}}$ is an effective Hund's coupling trying to align spin directions in all orbitals. The model in Eq. (C4) goes back to the one in Eq. (C3) in the limit $\tilde{J}_{\text{H}} \to \infty$. By reducing the value of $\tilde{J}_{\text{H}}$, the effects from more low-spin configurations are taken into account.

To precisely determine the values of the model parameters $\tilde{J}_{\text{H}}$ and $J_{ij}^{\alpha\beta}$ in Eq. (C4) requires accurate knowledge of $U$ and $J_{\text{H}}$ in the original multiorbital Hubbard model. We note that the purpose of the present work is to capture the key features of superconductivity over a wide physical regime of model parameters. As such, we further simplify the model in Eq. (C4) by taking $\tilde{J}_{\text{H}} = 0$. This makes the spin of each orbital independent, and maximally includes effects from low-spin states. In this way, we can project the effective Hamiltonian to each orbital subspace independently and determine the orbital dependent effective exchange couplings. For the in-plane nearest neighbor pair of sites, we find $J_1^{xx} = 158.6$ meV, $J_1^{zz} = 45.8$ meV, and $J_1^{zx} = -1.1$ meV for $U = 6$ eV and $J_{\text{H}}/U = 0.25$. The exchange couplings for a pair of sites along other directions are less than 1 meV in magnitude and are hence neglected. Note that for nearest neighbor pairs the intraorbital exchange couplings are both antiferromagnetic, whereas the interorbital one is very weakly ferromagnetic. This implies a strong competition between antiferromagnetic and ferromagnetic interorbital processes. Varying $U$ and $J_{\text{H}}/U$ can significantly modify the effective exchange couplings. In the calculation for superconductivity, we take $J_1^{zz} \approx 0.025W_0$ and leave $J_1^{xx}$ as a free parameter. Here $W_0 \sim 4$ eV is the bare bandwidth at $U = 0$.

[1] Y. Kamihara, T. Watanabe, M. Hirano, and H. Hosono, Iron-based layered superconductor La[$O_{1-x}F_x$]FeAs ($x = 0.05$-$0.12$) with $T_c = 26$ K, J. Am. Chem. Soc. **130**, 3296 (2008).

[2] D. C. Johnston, The puzzle of high temperature superconductivity in layered iron pnictides and chalcogenides, Adv. Phys. **59**, 803 (2010).

[3] Q. Si and N. E. Hussey, Iron-based superconductors: Teenage, complex, challenging, Phys. Today **76**(5), 34 (2023).

[4] H. Sun, M. Huo, X. Hu, J. Li, Z. Liu, Y. Han, L. Tang, Z. Mao, P. Yang, B. Wang, J. Cheng, D.-X. Yao, G.-M. Zhang, and M. Wang, Signatures of superconductivity near 80 K in a nickelate under high pressure, Nature (London) **621**, 493 (2023).

[5] J. Hou, P. T. Yang, Z. Y. Liu, J. Y. Li, P. F. Shan, L. Ma, G. Wang, N. N. Wang, H. Z. Guo, J. P. Sun, Y. Uwatoko, M. Wang, G.-M. Zhang, B. S. Wang, and J.-G. Cheng, Emergence

of high-temperature superconducting phase in the pressurized $La_3Ni_2O_7$ crystals, Chin. Phys. Lett. **40**, 117302 (2023).

[6] Y. Zhang, D. Su, Y. Huang, H. Sun, M. Huo, Z. Shan, K. Ye, Z. Yang, R. Li, M. Smidman, M. Wang, L. Jiao, and H. Yuan, High-temperature superconductivity with zero-resistance and strange metal behavior in $La_3Ni_2O_7$, arXiv:2307.14819.

[7] D. Li, K. Lee, B. Y. Wang, M. Osada, S. Crossley, H. R. Lee, Y. Cui, Y. Hikita, and H. Y. Hwang, Superconductivity in an infinite-layer nickelate, Nature (London) **572**, 624 (2019).

[8] Z. Luo, X. Hu, M. Wang, W. Wu, and D.-X. Yao, Bilayer two-orbital model of $La_3Ni_2O_7$ under pressure, Phys. Rev. Lett. **131**, 126001 (2023).

[9] Y. Gu, C. Le, Z. Yang, X. Wu, and J. Hu, Effective model and pairing tendency in bilayer Ni-based superconductor $La_3Ni_2O_7$, arXiv:2306.07275.

[10] V. Christiansson, F. Petocchi, and P. Werner, Correlated electronic structure of $La_3Ni_2O_7$ under pressure, Phys. Rev. Lett. **131**, 206501 (2023).

[11] Q.-G. Yang, D. Wang, and Q.-H. Wang, Possible $S_{\pm}$-wave superconductivity in $La_3Ni_2O_7$, Phys. Rev. B **108**, L140505 (2023).

[12] F. Lechermann, J. Gondolf, S. Bötzel, and I. M. Eremin, Electronic correlations and superconducting instability in $La_3Ni_2O_7$ under high pressure, Phys. Rev. B **108**, L201121 (2023).

[13] Y. Shen, M. Qin, and G.-M. Zhang, Effective bi-layer model Hamiltonian and density-matrix renormalization group study for the high-$T_c$ superconductivity in $La_3Ni_2O_7$ under high pressure, Chin. Phys. Lett. **40**, 127401 (2023).

[14] D. A. Shilenko and I. V. Leonov, Correlated electronic structure, orbital-selective behavior, and magnetic correlations in double-layer $La_3Ni_2O_7$ under pressure, Phys. Rev. B **108**, 125105 (2023).

[15] Y. Zhang, L.-F. Lin, A. Moreo, and E. Dagotto, Electronic structure, orbital-selective behavior, and magnetic tendencies in the bilayer nickelate superconductor $La_3Ni_2O_7$ under pressure, Phys. Rev. B **108**, L180510 (2023).

[16] H. Sakakibara, N. Kitamine, M. Ochi, and K. Kuroki, Possible high $T_c$ superconductivity in $La_3Ni_2O_7$ under high pressure through manifestation of a nearly-half-filled bilayer Hubbard model, arXiv:2306.06039.

[17] A. Yang, X. Tao, Y. Quan, and P. Zhang, A first-principles investigation of the origin of superconductivity in $TlBi_2$, Phys. Rev. B **108**, 075203 (2023).

[18] X. Chen, P. Jiang, J. Li, Z. Zhong, and Y. Lu, Critical charge and spin instabilities in superconducting $La_3Ni_2O_7$, arXiv:2307.07154.

[19] Y.-B. Liu, J.-W. Mei, F. Ye, W.-Q. Chen, and F. Yang, $s^{\pm}$-wave pairing and the destructive role of apical-oxygen deficiencies in $La_3Ni_2O_7$ under pressure, Phys. Rev. Lett. **131**, 236002 (2023).

[20] Y. Cao and Y.-F. Yang, Flat bands promoted by Hund's rule coupling in the candidate double-layer high-temperature superconductor $La_3Ni_2O_7$, arXiv:2307.06806.

[21] W. Wu, Z. Luo, D.-X. Yao, and M. Wang, Charge transfer and Zhang-Rice singlet bands in the nickelate superconductor $La_3Ni_2O_7$ under pressure, arXiv:2307.05662.

[22] C. Lu, Z. Pan, F. Yang, and C. Wu, Interlayer coupling driven high-temperature superconductivity in $La_3Ni_2O_7$ under pressure, arXiv:2307.14965.

[23] Z. Liu, M. Huo, J. Li, Q. Li, Y. Liu, Y. Dai, X. Zhou, J. Hao, Y. Lu, M. Wang, and H.-H. Wen, Electronic correlations and energy gap in the bilayer nickelate $La_3Ni_2O_7$, arXiv:2307.02950.

[24] C. Castellani, C. R. Natoli, and J. Ranninger, Magnetic structure of $V_2O_3$ in the insulating phase, Phys. Rev. B **18**, 4945 (1978).

[25] R. Yu and Q. Si, $U(1)$ slave-spin theory and its application to Mott transition in a multiorbital model for iron pnictides, Phys. Rev. B **86**, 085104 (2012).

[26] R. Yu and Q. Si, Orbital-selective Mott phase in multiorbital models for iron pnictides and chalcogenides, Phys. Rev. B **96**, 125110 (2017).

[27] K. I. Kugel and D. I. Khomskii, Sov. Phys. Usp. **25**, 231 (1982).

[28] P. A. Lee, N. Nagaosa, and X.-G. Wen, Doping a Mott insulator: Physics of high-temperature superconductivity, Rev. Mod. Phys. **78**, 17 (2006).

[29] R. Yu, P. Goswami, Q. Si, P. Nikolic, and J.-X. Zhu, Superconductivity at the border of electron localization and itinerancy, Nat. Commun. **4**, 2783 (2013).

[30] H. Hu, R. Yu, E. M. Nica, J.-X. Zhu, and Q. Si, Orbital-selective superconductivity in the nematic phase of FeSe, Phys. Rev. B **98**, 220503(R) (2018).

[31] R. Yu and Q. Si, Orbital-selective Mott phase in multiorbital models for alkaline iron selenides $K_{1-x}Fe_{2-y}Se_2$, Phys. Rev. Lett. **110**, 146402 (2013).

[32] M. Yi, Z.-K. Liu, Y. Zhang, R. Yu, J.-X. Zhu, J. J. Lee, R. G. Moore, F. T. Schmitt, W. Li, S. C. Riggs *et al.*, Observation of universal strong orbital-dependent correlation effects in iron chalcogenides, Nat. Commun. **6**, 7777 (2015).

[33] J. Huang, R. Yu, Z. Xu, J.-X. Zhu, J. S. Oh, Q. Jiang, M. Wang, H. Wu, T. Chen, J. D. Denlinger *et al.*, Correlation-driven electronic reconstruction in $FeTe_{1-x}Se_x$, Commun. Phys. **5**, 29 (2022).

[34] G. Wu, J. J. Neumeier, and M. F. Hundley, Magnetic susceptibility, heat capacity, and pressure dependence of the electrical resistivity of $La_3Ni_2O_7$ and $La_4Ni_3O_{10}$, Phys. Rev. B **63**, 245120 (2001).

[35] Z. Liu, H. Sun, M. Huo, X. Ma, Y. Ji, E. Yi, L. Li, H. Liu, J. Yu, Z. Zhang, Z. Chen, F. Liang, H. Dong, H. Guo, D. Zhong, B. Shen, S. Li, and M. Wang, Evidence for charge and spin density waves in single crystals of $La_3Ni_2O_7$ and $La_3Ni_2O_6$, Sci. China Phys. Mech. Astron. **66**, 217411 (2023).

[36] See VASP website, https://www.vasp.at/.

[37] G. Pizzi *et al.*, Wannier90 as a community code: new features and applications, J. Phys.: Condens. Matter **32**, 165902 (2020).